Astron. Astrophys. 345, 369–379 (1999)

ASTRONOMY AND ASTROPHYSICS

CO lines in high redshift galaxies: perspective for future mm instruments

F. Combes[1], **R. Maoli**[1,2], **and A. Omont**[2]

[1] Observatoire de Paris, DEMIRM, 61 Av. de l'Observatoire, F-75014 Paris, France
[2] Institut d'Astrophysique de Paris-CNRS, 98 bis Bd. Arago, F-75014 Paris, France

Received 4 November 1998 / Accepted 1 March 1999

Abstract. Nearly 10 high redshift ($z > 2$) starburst galaxies have recently been detected in the CO lines, revealing the early presence in the universe of objects with large amounts of already-enriched molecular gas. The latter has sufficient density to be excited in the high-level rotational CO lines, which yield more flux than low-level lines, making easier high-redshift detections; however there is no negative K-correction as for the sub-millimeter and far-infrared dust continuum emission. With the help of simple galaxy models, based on these first detections, we estimate the flux in all CO lines expected for such starbursting objects at various redshifts. We discuss the detection perspectives with the future millimeter instruments.

Key words: galaxies: ISM – galaxies: starburst – cosmology: observations – radio continuum: galaxies – radio lines: galaxies – submillimeter

1. Introduction

The detection of high-redhifted ($z > 2$) millimeter CO lines in the hyperluminous object IRAS 10214+4724 ($z = 2.28$, Brown & Vanden Bout 1992, Solomon et al. 1992a), has opened a new way of research to tackle the star formation history of the Universe. Although the object turned out to be highly gravitationally amplified, it revealed however that galaxies at this epoch could have large amounts of molecular gas, excited by an important starburst, and sufficiently metal-enriched to emit detectable CO emission lines. The latter bring fundamental information about the cold gas component in high-z objects and therefore about the physical conditions of the formation of galaxies and the first generations of stars. At high enough redshifts, most of the galaxy mass could be molecular. The main problem to detect this molecular component could be its low metallicity, but theoretical calculations have shown that in a violent starburst, the metallicity could reach solar values very quickly (Elbaz et al. 1992).

After the first discovery, many searches for other candidates took place, but they were harder than expected, and only a few, often gravitationally amplified, objects have been detected: the lensed Cloverleaf quasar H 1413+117 at $z = 2.558$ (Barvainis et al. 1994), the lensed radiogalaxy MG0414+0534 at $z = 2.639$ (Barvainis et al. 1998), the possibly magnified object BR1202-0725 at $z = 4.69$ (Ohta et al. 1996, Omont et al. 1996a), the amplified submillimeter-selected hyperluminous galaxies SMM02399-0136 at $z = 2.808$ (Frayer et al. 1998), and SMM 14011+0252 at 2.565 (Frayer et al. 1999), and the magnified BAL quasar APM08279+5255, at $z = 3.911$, where the gas temperature derived from the CO lines is ~ 200 K, maybe excited by the quasar (Downes et al. 1999). Recently Scoville et al. (1997b) reported the detection of the first non-lensed object at $z = 2.394$, the weak radio galaxy 53W002, and Guilloteau et al. (1997) the radio-quiet quasar BRI 1335-0417, at $z = 4.407$, which has no direct indication of lensing. If the non-amplification is confirmed, these objects would contain the largest molecular contents known (8–10 10^{10} $M_\odot$ with a standard CO/H_2 conversion ratio, and even more if the metallicity is low). The derived molecular masses are so high that H_2 would constitute between 30 to 80% of the total dynamical mass (according to the unknown inclination), if the standard CO/H_2 conversion ratio was adopted. The application of this conversion ratio is however doubtful, and it is possible that the involved H_2 masses are 3–4 times lower (Solomon et al. 1997).

Obviously, the search of CO lines in high-z objects is still a challenge for present day instrumentation, but this will rapidly change with the new millimeter instruments planned over the world (the Green-Bank-100m of NRAO, the LMT-50m of UMass-INAOE, the LSA-MMA (Europe/USA) and the LMSA (Japan) interferometers). It is therefore interesting to predict with simple models the detection capabilities, as a function of redshift, metallicity or physical conditions in the high-z objects. In particular, it would be highly interesting to detect not only the few exceptional amplified monsters in the sky, but also the widely spread normal galaxy population of the young universe. Our aim here is to determine to which redshift it will be possible, and with which instrument. A previous study has already modelled galaxies at very high redshift (up to $z = 30$) and concluded that CO lines could be even more easy to detect than the continuum (Silk & Spaans 1997). Our models do not agree with this conclusion.

Sect. 2 describes the two-component model we use for the molecular clouds of the starburst galaxies, Sect. 3 the cosmological model; both are combined and the results are discussed

Send offprint requests to: F. Combes

Table 1. CO data for high redshift objects

Source	z	CO line	S mJy	ΔV km s^{-1}	MH$_2$ 10^{10} M$_\odot$	Ref
F10214+4724	2.285	3-2	18	230	2*	1
53W002	2.394	3-2	3	540	7	2
H 1413+117	2.558	3-2	23	330	2-6	3
SMM 14011+0252	2.565	3-2	13	200	5*	4
MG 0414+0534	2.639	3-2	4	580	5*	5
SMM 02399-0136	2.808	3-2	4	710	8*	6
APM 08279+5255	3.911	4-3	6	400	0.3*	7
BR 1335-0414	4.407	5-4	7	420	10	8
BR 1202-0725	4.690	5-4	8	320	10	9

* corrected for magnification, when estimated
Masses have been rescaled to H_0 = 75 km s^{-1}/Mpc. When multiple images are resolved, the flux corresponds to their sum
(1) Solomon et al. (1992a), Downes et al. (1995); (2) Scoville et al. (1997b); (3) Barvainis et al. (1994, 1997); (4) Frayer et al. (1999); (5) Barvainis et al. (1998); (6) Frayer et al. (1998); (7) Downes et al. (1999); (8) Guilloteau et al. (1997); (9) Omont et al. (1996a)

Table 2. Parameters of the two-component model

Parameter	Hot comp.	Warm comp.
n(H$_2$) cm^{-3}	10^6	10^4
sizes (pc)	0.1	1
ΔV (km s^{-1})	10	10
T_K (z = 0.1)	90.0	30.0
T_K (z = 1.0)	90.0	30.0
T_K (z = 2.0)	90.0	30.0
T_K (z = 3.0)	90.0	30.0
T_K (z = 5.0)	90.0	30.1
T_K (z = 10.0)	90.0	33.7
T_K (z = 20.0)	91.0	57.5
T_K (z = 30.0)	98.2	84.6
N(CO) cm^{-2}	3. 10^{19}	3. 10^{18}
N(H$_2$) cm^{-2}	3. 10^{23}	3. 10^{22}
f$_s^*$	1.	100.
f$_v^*$	0.03	0.03
mass fraction	0.1	0.9

* f$_s$: surface filling factor, f$_v$ velocity filling factor
T_K increases with z keeping $T_{dust}^6 - T_{bg}^6$ constant (see text)

in Sect. 4. Sect. 5 describes the detection perspectives with the future millimeter instruments.

2. Galaxy ISM modeling

Since the physical conditions of the interstellar medium is still unknown in early galaxies, the most straightforward modeling is to extrapolate what we know from the local star-forming clouds in the Milky Way. Solomon et al. (1990) showed that the ISM of ultra-luminous starbursting galaxies is likely to contain a large fraction of dense gas, corresponding to the star-forming cores of local molecular clouds. The gross features of the CO and far-infrared emissions of these luminous starbursts can be explained by a dense (average density 10^4 cm^{-3}) molecular component confined in the central kpc, containing cores of even higher density ($\sim 10^6$ cm^{-3}). These are about 100 times denser than in a normal galactic disk. The FIR to CO luminosity ratio are nearly those expected for an optically thick region radiating as a black-body (Solomon et al. 1997). Typical masses of molecular gas are 2–6 10^{10} M$_\odot$.

The dominant dust component in ultra-luminous galaxies has a temperature between 30 and 50 K, while there is sometimes a higher temperature emission bump (e.g. Klaas et al. 1997). The emission peaks around 100 μm with a flux of 1–3 Jy at $z = 0.1$. At the higher redshifts of $z = 4$–5, continuum fluxes of a few mJy have been detected at 1.25mm (e.g. Omont et al. 1996b), corresponding to dust emission at about 220 μm, with gas masses up to 10^{11} M$_\odot$ if no gravitational lens is present. As for the CO lines, they are more difficult to detect with present day instrumentation, and most of the 8 detections reported so far are gravitationally magnified. The flux detected range between 3 to 20 mJy for lines (3–2) to (7–6) (see Table 1).

A striking feature of these ultra-luminous infra-red objects, is that both the IR and CO emissions originate in regions a few hundred parsecs in radius (Scoville et al. 1997a, Solomon et al. 1997, Barvainis et al. 1997). Observations at arcsecond resolution have shown that the molecular gas is confined in compact sub-kpc components, or disks of a few hundred parsecs in radius. The average H_2 surface density there is of the order of a few 10^{24} cm^{-2} (Bryant & Scoville 1996). The gas must be clumpy, since molecules with high dipole moment are excited, such as HCN (Solomon et al. 1992b). This strong central concentration corresponds very well to what is expected in a merger by N-body simulations (e.g. Barnes & Hernquist 1992). Due to gas dissipation and gravity torques, large H_2 concentrations pile up at the galaxy nuclei in interacting systems. Up to 50% of the dynamical mass could be under the form of molecular hydrogen in mergers (Scoville et al. 1991). The most extreme ultra-luminous infrared galaxies, which are also mergers and starbursts possess several 10^{10} M$_\odot$ of H_2 gas, more than 10 times the H_2 content of the Milky Way.

2.1. A two-component model

We will therefore base our simple model on a small inner disk of 1 kpc diameter, containing two density components (cf Table 2). Both are distributed in clouds of low volume filling factor. The dense and hot component represents the star-forming cores, and for the sake of simplicity, there is one core in every cloud. Because of the large velocity gradients in the inner regions (due to rotation or macroscopic velocity dispersion), most of these cores are not overlapping at a given velocity, and their molecular emission can be simply summed up. This is not the case for the more extended clouds (see below), or for the dust, that could be optically thick at some frequencies. For the opacity of the dust, we take the formula computed by Draine & Lee (1984) and quite compatible with observations (see Boulanger et al. 1996):

$\tau = N_H(cm^{-2})10^{-25}(\lambda/250\,\mu)^2$

The total molecular mass is chosen to be 6 10^{10} $M_\odot$, and the average column density N(H_2) of the order of 10^{24} cm^{-2} (typical of the Orion cloud center). To fix ideas, we assume that the total mass is distributed in 8.6 10^7 clouds of 700 $M_\odot$ each, with an individual velocity dispersion of 10 km s^{-1}, embedded in a macroscopic profile of 300 km s^{-1} dispersion/rotation (cf Table 2). The column density of each cloud is respectively 3 10^{22} cm^{-2} for the extended component and 3 10^{23} cm^{-2} for the core. For the sake of simplicity, we consider cubic clouds (the cube size is indicated in Table 2), and their mass is computed taking into account the helium mass (total mass larger than the H_2 mass by a factor 1.33).

As for the temperatures of the two components, we choose for local clouds T_K = 30 K for the extended component, and 90 K for the star-forming cores. We do not take into account here a hotter component, possibly heated by the AGN, as seen in F10214+4724 (Downes et al. 1995) or the Cloverleaf (Barvainis et al. 1997). These temperatures were increased at high redshift, to take into account the hotter cosmic background: indeed the dust is heated above the background temperature by the UV and visible light coming from the stars. Assuming the same star-formation rate for the clouds, and the same fraction of the star light reprocessed by the optically thin dust, with an opacity varying as λ^{-2}, the quantity $T^6_{dust} - T^6_{bg}$ is fixed. This means that the difference between the energy re-radiated by the dust ($\propto T^6_{dust}$), and the energy received from the cosmic background by the dust ($\propto T^6_{bg}$) is always the same. This is the energy flux coming from the stars. We assume that the density is so high that the gas is heated efficiently by the dust, and T_{dust} = T_K (which maximises the line flux). This condition might not be satisfied, and our CO line fluxes from the gas could be somewhat optimistic (however not by a large factor). The corresponding temperatures as a function of redshift are displayed in Table 2. We have also varied this condition, to take into account other dust properties: in some dust infra-red spectra, the opacity dependence with frequency has a lower power than ν^2 (sometimes $\nu^{1.5}$ or ν); also the dust could be completely optically thick, so that the quantity $T^4_{dust} - T^4_{bg}$ is conserved. This relation gives the maximum possible temperatures, and the results are discussed below. With these two simple models, the dust temperatures are bracketed.

We compute the relative populations of the CO molecule levels in each component with the LVG approximation (using 17 levels); results are displayed in Fig. 1, for each temperature component. At each redshift, the actual level populations are plotted as a full line, and the LTE distribution as a dotted line for comparison. At high temperature, the full and dotted lines coincide. From these distributions, excitation temperatures T_{ex} and opacities τ can be derived for each CO line, and summed with the relevant filling factors for the two components. Antenna temperatures are obtained through

$$T_A = [f(T_{ex}) - f(T_{bg})][1 - exp(-\tau)] \quad (1)$$

where $f(T) = \frac{h\nu}{k}(exp(\frac{h\nu}{kT}) - 1)^{-1}$. The flux is then

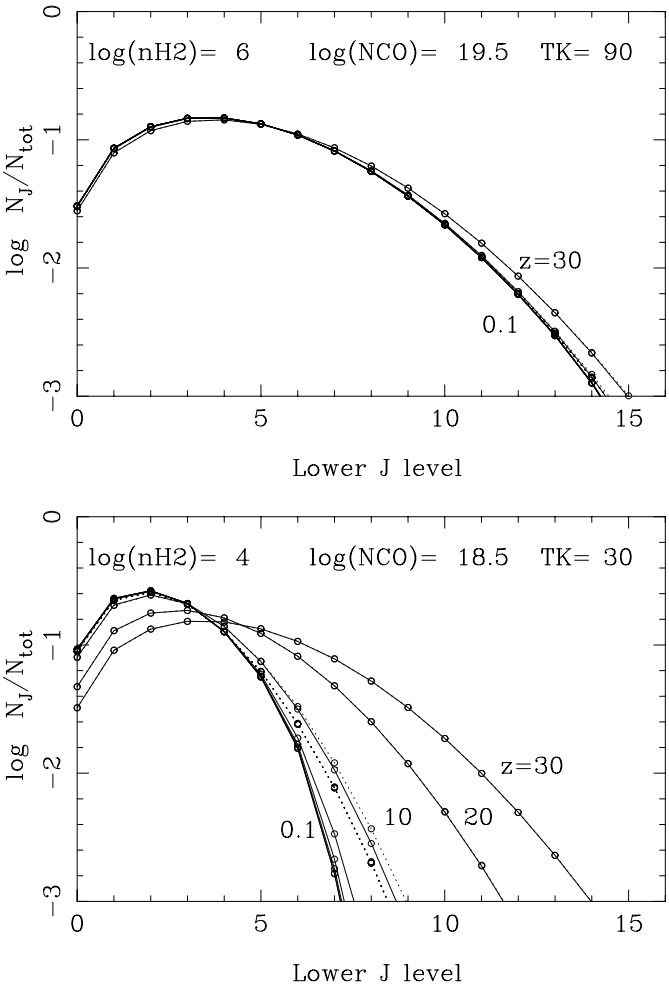

Fig. 1. Relative populations of the CO molecules, for the hot core (upper) and warm cloud (bottom) components. The 8 curves correspond to redshifts z= 0.1, 1, 2, 3, 5, 10, 20, 30. The values of T_K indicated are for z= 0 (see Table 2), and they do not vary up to z = 5. The full curves are the actual distributions, and the dotted curves correspond to the LTE ones, at the corresponding T_K (cf Table 2). The 5 first dotted curves are superposed (same T_K), and the two last ones (z = 20 and 30) are coinciding with their corresponding full curves.

$$S = \frac{2kT_A}{\lambda^2}\Omega_S \quad (2)$$

where Ω_S is the angular size of the source.

The emission from individual clouds are summed directly, as long as their total filling factor (i.e. the product of the surface and velocity filling factor for the lines, or only the surface filling factor for the continuum) is smaller than 1. When the total filling factor is larger than 1, the overlapping of clouds is taken into account, and the opacity is increased on each line of sight by this factor. This takes into account the overcrowding and self-absorption of the cloud population. We computed the equivalent CO to H_2 conversion factor in this model, for the CO(1-0) flux at $z = 0.1$: it is X= 5 10^{20} mol/K/km.s^{-1}. At higher redshift, X increases, since the gas is hotter and the emission comes out in higher-J lines than CO(1-0); it is 9 10^{20} at $z = 5$ and 280 10^{20} at $z = 30$.

2.2. An homogeneous sphere model

We also computed a quite different model of the molecular gas in starburst, a homogeneous sphere model. This is motivated by the consideration that the tidal forces and star formation energy could be so high in the center as to disrupt molecular clouds. The CO to H_2 conversion factor could then be quite different from the standard one, based on a collection of virialised clouds. The total mass and size is the same in this model: 6 10^{10} $M_\odot$ and 1 kpc diameter. The unique temperature is chosen to be T_d = 50 K. Since the surface density of the homogeneous source is 3.5 10^{24} cm^{-2}, the dust is optically thick for wavelengths $\lambda <$ 150 μm, and the emission of the central molecular region can be approximately modelled by a black-body (e.g. Solomon et al. 1997). The average density is however 10^3 cm^{-3}, not enough to reach LTE even in the low levels. The LVG model yields in this case an excitation temperature approaching T_K for the first CO levels, then decreasing to a minimum, that could be 3 times below, and increasing slightly for the highest levels (this translates into oscillations of the flux versus wavelength, as shown in Fig. 7 below). The equivalent CO to H_2 conversion factor in this model, for the CO(1-0) flux at z = 0.1, is now X= 3.7 10^{20} mol/K/km.s^{-1} (5.1 10^{20} at z = 5 and 370 10^{20} at z = 30).

It must be noted that the homogeneous gas model minimises the optical depth of the CO lines, at a given velocity, since both the spatial and velocity filling factors are 1, and consequently, it should maximise the amount of CO emission per gas mass. However, since the corresponding density is then small (here 10^3 cm^{-3}), the rotational levels are not excited to a J as high as in the two-component clumpy model, and the excitation temperature is less than the kinetic temperature (cf Fig. 2). This reduces the efficiency of the CO lines emission. One way to have a better emissivity is to enlarge the starburst region to a size of several kpc, but this is not likely to occur, given the observations of ultra-luminous galaxies at low redshift, and the huge star formation rate then required.

In summary, the clumpy and homogeneous models are two extreme simple models that help us to explore the large range of cloud distribution possibilities.

The principal way to optimize CO lines emissivity is to assume that they are never highly optically thick, as assumed by Barvainis et al. (1997). In their first interpretation of the CO lines from the Cloverleaf, Barvainis et al. (1994) derived an H_2 mass of 4 10^{11} $M_\odot$ (uncorrected for magnification), about an order of magnitude larger than in Barvainis et al. (1997). In the latter work, the authors claim that the optical depth of the CO lines cannot be much larger than 1, since the CO line ratios between the (3–2), (4–3), (5–4) and (7–6) lines would then be Rayleigh-Jeans (in ν^2), which is not confirmed by observations. However, the various rotational lines might not come from the same area, and their relative magnification ratios are unknown. This prevents a definite conclusion about the optical depth of the lines. Let us note that the low-optical depth models are rather contrived, since to have a high enough excitation, the density must be substantial, while the column density must be kept low.

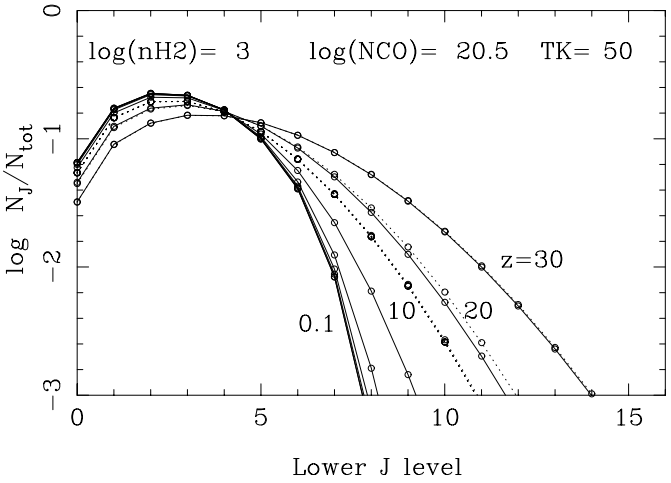

Fig. 2. Same as Fig. 1, for the homogeneous sphere model, at T_K = 50 K, at z = 0. The 6 first dotted curves are superposed (same T_K), and the two last ones (z = 20 and 30) are almost coinciding with their corresponding full curves.

This results for instance in clumps of 0.1pc size for instance, in the T = 60 K model of Barvainis et al. (1997), that completely cover the source surface (with a low volume filling factor). To reach a diffuse homogeneous sphere, the temperature should be larger than T = 300 K (but then the expected dust emission is too large).

In our standard two-component clumpy model, the low-J lines are highly optically thick ($\tau \geq 100$), and their relative intensities are in the Rayleigh-Jeans ratio. We explore the optically thin cases in Sect. 4, and in particular study the evolution of the continuum-to-line ratio.

3. Cosmological model

For very distant ($z > 1$) objects, the luminosity and angular size distances are significantly different (cf examples in Fig. 3). We parametrize as usual the cosmological model by the Hubble constant H_0 (here fixed to 75 km s^{-1}/Mpc), and the deceleration parameter q_0. We choose two values q_0= 0.1 and 0.5 to illustrate our computations here, corresponding respectively to an open universe, and to a critical (Einstein-deSitter model) flat one, for a zero cosmological constant (since in this case $\Omega_0 = 2\,q_0$). For a matter-dominated Friedmann universe, the luminosity distance of an object at redshift z is (e.g. Weinberg 1972):

$$D_L = \frac{c}{H_0 q_0^2}\left[z q_0 + (q_0 - 1)\left(-1 + \sqrt{2 q_0 z + 1}\right)\right] \qquad (3)$$

and the angular size distance:

$$D_A = (1+z)^{-2} D_L \qquad (4)$$

As can be seen in Fig. 3, the latter is decreasing with z as soon as $z > 2$, i.e. the apparent diameter of objects increase with z. This may give the spurious impression that sources at high redshift will be more easy to detect; in fact the measured integrated flux decreases as D_L^2. It is interesting to introduce the correction

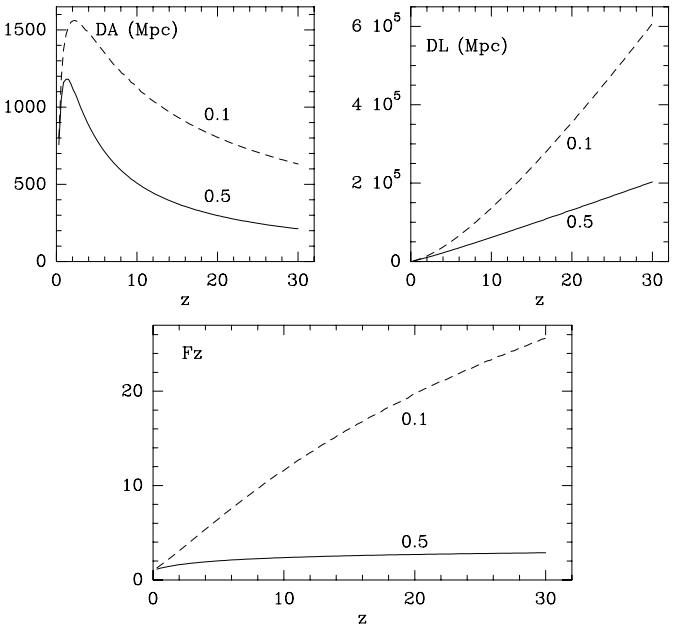

Fig. 3. Angular size distance (D_A), luminosity distance (D_L) and correction factor $F_z = (\frac{D_L H_0}{cz})^2$, for two values of q_0 (0.5 full line, 0.1 dashed line).

factor F_z, which is the square of the ratio of the luminosity distance to the extrapolation of the low-redshift distance formula cz/H_0 (see for instance Gordon et al. 1992):

$$F_z = \left(\frac{D_L H_0}{cz}\right)^2 \quad (5)$$

This correction factor is also plotted in Fig. 3, and is varying almost as z for $q_0 = 0.1$. This means that for a given intrinsic luminosity, this factor makes it more and more difficult to detect objects at high redshift. The only favorable factor in the millimetric domain is what is usually called "a negative K-correction"[1], i.e. that the flux of the object increases with the frequency ν faster than ν^2 in the wavelength domain considered, and therefore that its apparent luminosity could increase with redshift. This is occuring for the dust emission from starbursts, which peaks in the 60–100 μm region, and is progressively redshifted in the submillimeter and millimeter domain, where it is as easy to detect objects at $z = 5$ than $z = 1$ (Blain & Longair 1993, McMahon et al. 1994, Omont et al. 1996b, Hughes et al. 1998).

To estimate detection capabilities, we will consider only point sources, for the sake of simplicity. At $z = 2$, a beamwidth of 1″, reached already by present mm interferometers, encompasses about 7 kpc, which is much larger than the area of dense and excited molecular gas in a starburst. With the foreseen next generation mm instruments, it will be possible to begin to resolve the emission only for the best possible resolution (0.1″) and for very large redshifts, if however there is enough sensitivity.

At the present time, galaxies are detected in the optical up to $z = 6$ only. At this epoch, the age of the universe is about 5% of its age, or 10^{10} yrs in a standard flat model. For larger redshifts, it is likely that the total amount of cumulated star formation is not a significant fraction of the total (e.g. Madau et al. 1996). However, it is of overwhelming interest to trace the first star-forming structures, as early as possible to constrain theories of galaxy formation. At the recombination of matter, at $z \sim 1000$, the first structures to become unstable have masses between 10^5 and 10^8 $M_\odot$, and at $z \sim 30$, it is possible that some structures of 10^{10}-10^{12} $M_\odot$ become in turn non linear, according to models, so we have computed our estimations until such extreme redshifts (~ 30), even if such massive objects are not likely to be numerous so early.

4. Results and discussion

4.1. The standard clumpy model

The computed flux in the CO lines (not integrated in frequency) for the two-component cloud model is shown in Fig. 4 for the 8 values of the redshift considered. The two temperature contributions can be seen clearly, although they tend to merge at high redshift. The effect of the assumption on the gas temperatures can be seen by comparison with Fig. 5, which maximises the gas temperatures. We can see at once that the largest sensitivity for CO detection is around the lines CO(6-5) or CO(5-4) for the redshift up to z = 5. At larger redshifts, the higher lines CO(15-14) or CO(14-13) will be the best choice, in the 3–5mm domain.

The first effect to notice is the strong negative K-correction in the dust emission, which makes its detection even more easy at z = 5 or 1. For a fixed wavelength range, for instance at 3mm, we see that the various redshift curves of Fig. 4 are almost touching each other, or are even z-reversed. However, the effect is much more favorable for continuum detection. For CO lines, we see more precisely that there is a factor 3 in flux between these two redshifts (z = 1 and 5) for a given λ, and therefore that ten times more integration time is required to detect the same objects at z = 5 with respect to z = 1. This difference between the lines and continuum comes from the fact that the lines are highly optically thick at long wavelengths: the right side of the curves in Fig. 4 for the lines go as λ^{-2} (the Rayleigh Jeans approximation), while for the continuum, they go as λ^{-4}, due to the dust opacity in ν^2, and the fact that at low redshift and at these long wavelengths the dust is optically thin. The K-correction advantage is then much stronger for the dust emission; it is even optimum at very high redshift (z = 10 to 30), since the maximum dust emission then enters the mm domain, and begins to be optically thick.

Fig. 4 demonstrates that it is easier to detect the dust emission of starbursts at $z > 10$ than at z = 5, at 1mm, and therefore it should be possible to detect them with today instruments. How-

[1] The term of K correction may appear confusing; it has been used for the first time by Wirtz in 1918, for "Kosmologie" to determine the distance-redshift law; Hubble (1929) called also K (after Wirtz's law) his now famous constant, and Oke & Sandage (1968) quantified what they called the K-correction, the combined effet of the changing λ domain (if the spectrum of the object is not flat), and the reduced λ-interval observed at high redshift, given a photometry band.

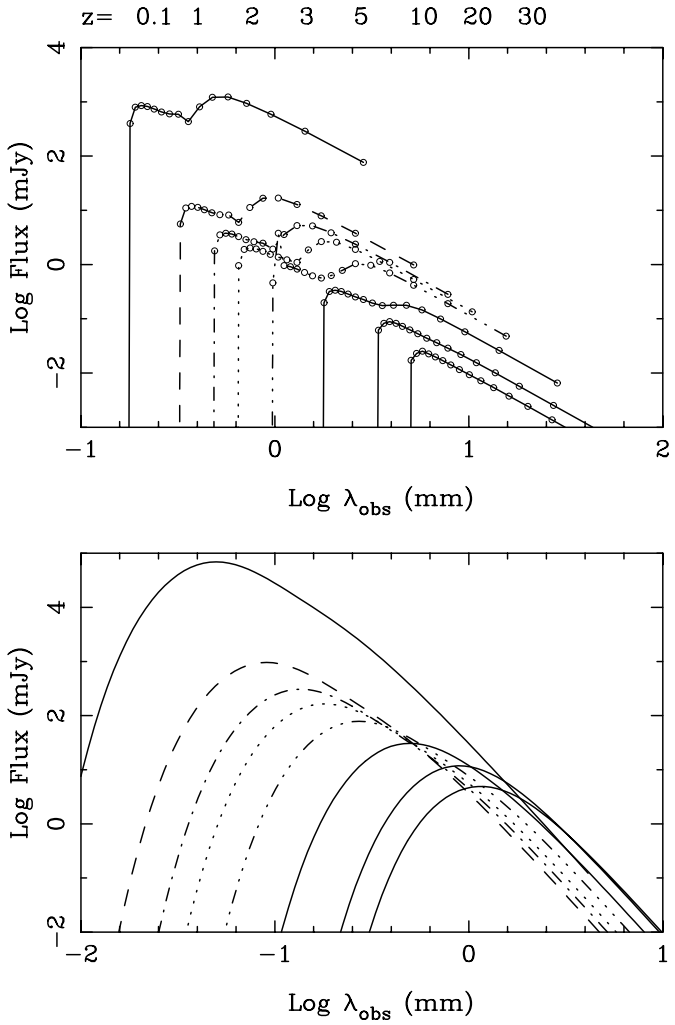

Fig. 4. Expected flux for the two-component cloud model, for various redshifts z = 0.1, 1, 2, 3, 5, 10, 20, 30, and q_0 = 0.5. Top are the CO lines, materialised each by a circle. Bottom is the continuum emission from dust. It has been assumed here that $T^6_{dust} - T^6_{bg}$ is conserved.

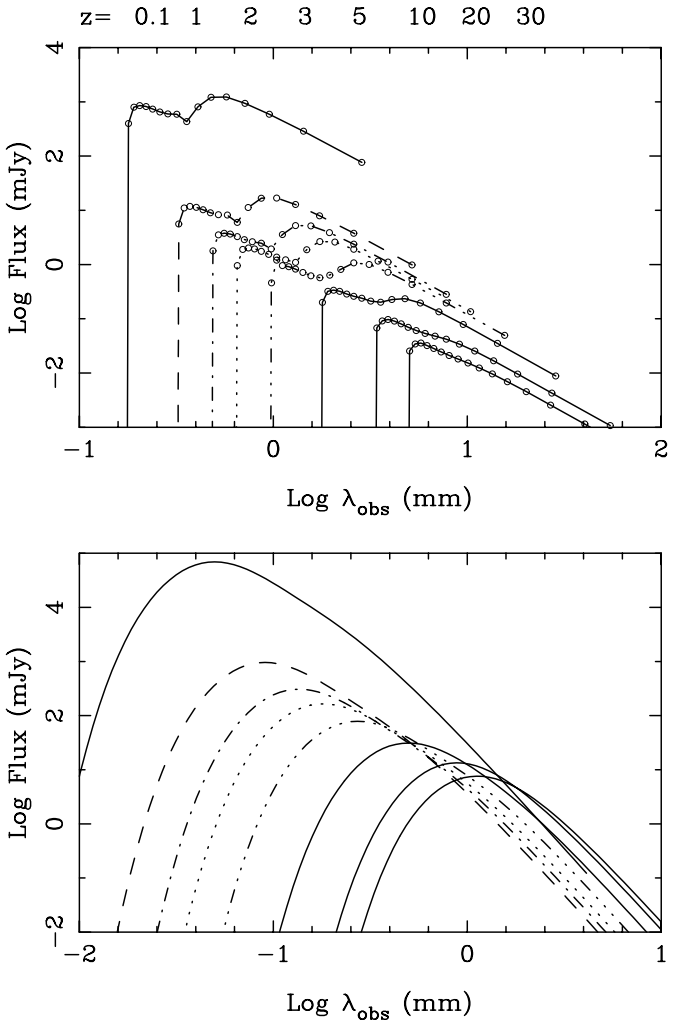

Fig. 5. Same as Fig. 4, but with $T^4_{dust} - T^4_{bg}$ conserved, as for an optically thick medium (see text for details).

ever all these estimates were computed for q_0 = 0.5. For q_0 = 0.1, the fluxes are smaller at high redshift, as indicated in Fig. 6.

A second obvious point to note, as far as the detection of CO lines at high-z is concerned, is that the maximum of emission is always at longer wavelengths than for the continuum (notice the different λ scales in Fig. 4). In the case of the CO lines, the emission peaks at a frequency lower by almost a factor 5 than in the case of the continuum. This is easy to understand, since it is the energy of the upper level J of the transition which corresponds to the gas temperature; this energy is proportional to $J(J+1)$. The energy of the transition is only a fraction of it, proportional to $2J$. Between the two, the ratio is almost a factor 5, in the case of the CO molecule, excited at a temperature of $\sim$ 90 K. The two peaks will be much closer for molecules of higher rotational energy, such as H_2O for instance, but their lines are expected to be much weaker and not as favorable for detection (because of clumpiness and high optical depth).

A question that could be asked is whether the hotter cosmic background at high z helps in the detection of the CO lines. It can be seen on the relative populations of CO levels (Fig. 1) that the density and column-densities we adopted for starburst objects are always high enough to excite the levels nearly thermally (almost LTE). The effect of going to high redshift does not play on excitation directly, but on the absolute temperature of the gas. The same effect occurs for the dust emission: temperatures are higher at high redshift, for the same star formation rate. But this does not help *in fine* on the detected flux level, since the observed flux takes into account the subtraction of the blackbody emission itself (cf Eq. (1)) which is also higher at high z. The net effect for lines is even negative, as shown in Fig. 4: the high-z curves drop down from the general tendency at lower redshift. This effect is generally ignored when such estimations are done, and this is justified for redshift ≤ 5 (e.g. Guiderdoni et al. 1998). Very often, for quick estimations, the curves of emission for a given object are simply redshifted (translated in log-log plots) to estimate the K-correction (e.g. Norman & Braun 1996, Israel & van der Werf 1996).

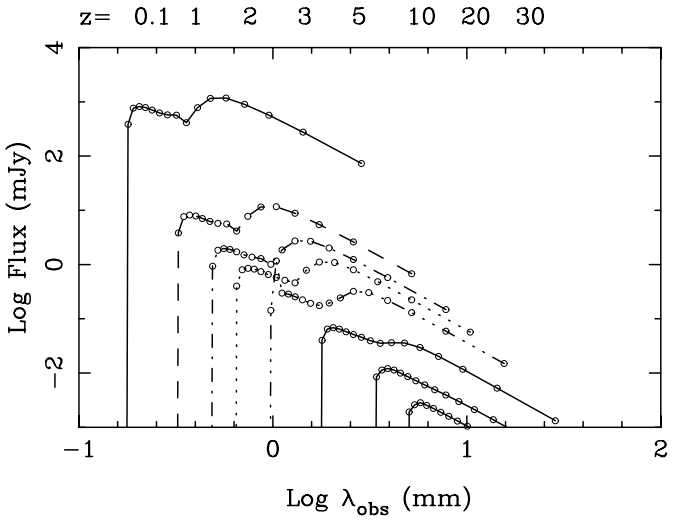

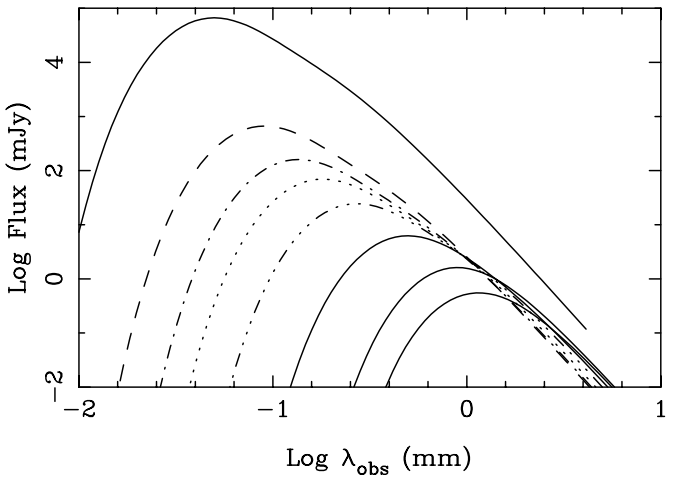

Fig. 6. Same as Fig. 4, but with q_0 = 0.1.

One can also take into account that it is the *integrated* flux which is relevant to detect a line, since smoothing proportionally to the line width increases the signal-to-noise. Because the width of the line (at constant ΔV) is proportional to the frequency ν, detection at high frequencies is then favored, as shown in Fig. 7.

4.2. The homogeneous model

In the case of the homogeneous sphere model, even though the CO to H_2 conversion factor is similar for the CO(1-0) line, our expectation to detect such objects at high-z is much less optimistic, because of the lower common temperature, and the lower excitation of the gas, which is now at low average density. The lines are significantly excited only up to the CO(6-5), and this reduces the flux at high redshift, for z = 20 and 30 (see Fig. 8). The dust emission is also considerably reduced at high redshift. Let us note that such low dust temperatures ($\leq 50\,K$) are relevant for a fraction of high-z sources such as BR1202-0725 (Benford et al. 1999), but not for others such as F10214+4724 (Downes et al. 1995), the Cloverleaf (Barvainis et al. 1997), or APM08279+5255 (Downes et al. 1999).

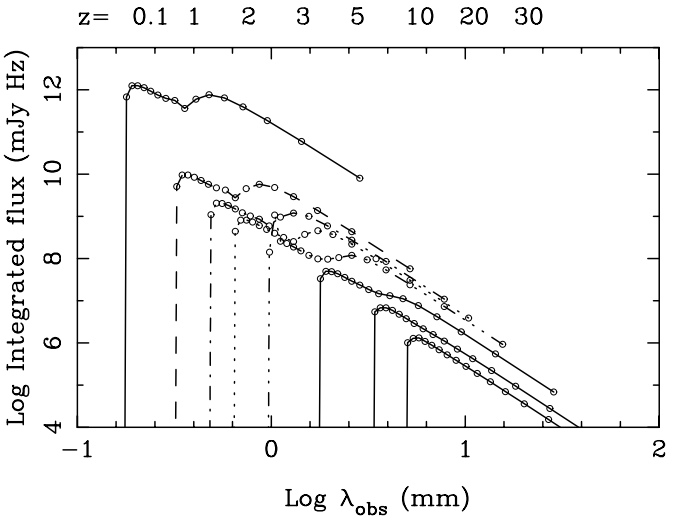

Fig. 7. Same as Fig. 4, but for the integrated flux, $\int S_\nu d\nu$, more relevant for detection.

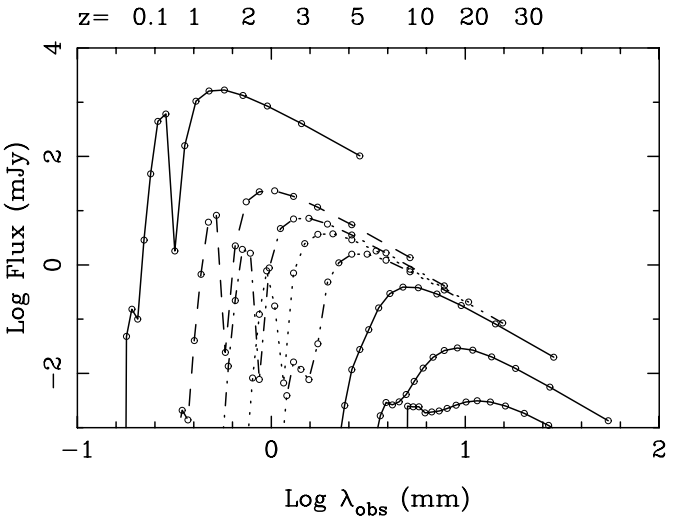

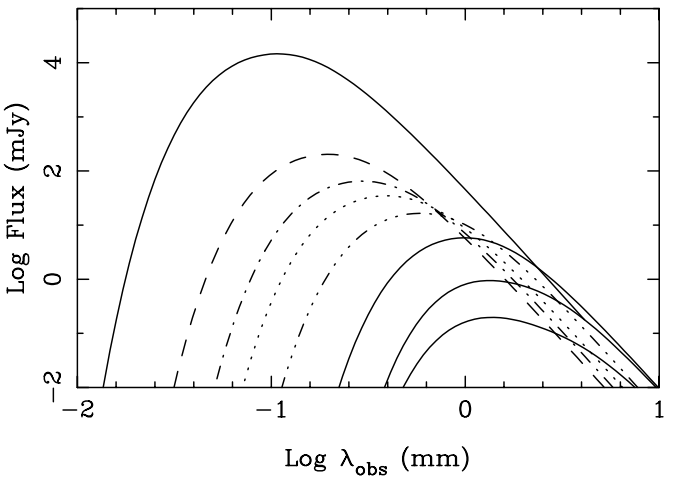

Fig. 8. Same as Fig. 4, but with the homogeneous sphere model, with T_d = 50 K. The non monotonous behaviour is due to excitation far from LTE (see Sect. 2.2)

4.3. Less optically thick models

The standard two-component clumpy model is optically thick in most CO lines. The optical depth comes essentially from the depth of the cloud components themselves, but also from the overlap of the clouds, at a given velocity. As can be seen in Table 2, the overlap amounts to $f_s f_v = 3$ for the warm component. It is therefore possible to have nearly the same CO emission for about 3 times less gas mass, at least for the low-J lines. The high-J line emission is provided mainly by the core component, for which there is no overlap ($f_s f_v = 0.03$). There is no significant absorption of the core emission by the warm component either, since at the high frequencies of the main core contribution, the warm component is optically thin. Therefore, dividing the total H_2 mass by 3, without modifying the cloud structure, will result in about the same low-J line emission, but 3-times less high-J emission. The continuum emission will also not be simply divided by 3 (since the dust $\tau \geq 1$ for $\lambda \leq 200$ μm), but its spectrum will change shape. It is interesting to plot the continuum-to-line ratio for the various cases. In Fig. 9, we plot both the total dimensionless L_{FIR}/L_{CO} ratio, where L_{CO} is integrated over all lines, and the L_{FIR}/L_{1-0} ratio, when only the CO(1-0) line is taken into account, as is done observationally (e.g. Solomon et al. 1997). We can see that both ratios increase with redshift, which confirms the fact that the continuum will be easier to detect at high z than the CO lines. The two cases, with 6 and 2 10^{10} $M_\odot$ of gas have not very different L_{FIR}/L_{CO} ratios (although the L_{FIR}/L_{1-0} ratio shows a marked effect, at low redshift).

Another obvious way to change the optical depth, without changing the cloud structure, is to change the metallicity, and consequently the CO and dust abundances. It is quite natural to keep the cloud structures (and their high H_2 density) for starburst objects; lower densities will not be able to excite the high-J CO lines, penalizing detectability at high z. It is, however, likely that gas at high z is less enriched in metals and dust. We have varied the CO/H_2 abundance ratio from 10^{-4} in the standard model to 10^{-8} by factors of 10, keeping the total gas mass at 6 10^{10} $M_\odot$. Fig. 9 summarizes the results. For lower metallicities, since both CO lines and dust are then entirely optically thin, the continuum-to-line ratio reaches a constant value, independent of total mass. It is nearly two orders of magnitude lower than in the standard model. Note that our models bracket the range of observed values. The standard model has a high ratio, due to its high gas mass, and high dust temperature (the ratio varies at least as T_d^3, and even more for moderate optical thickness).

The resulting spectra for the optically thin model, with CO/H_2 = 10^{-6}, are plotted in Fig. 10. The same behaviour as a function of redshift is observed, although the fluxes are lower, mainly in continuum.

4.4. Conclusion

In summary, we can see that the probability to detect objects at very high redshift is much larger in the continuum dust emission than in the CO lines. This is essentially due to a stronger K-correction advantage for the continuum, due to the lower opacity of dust. However, the detection of CO lines brings a lot of complementary information, involving the redshift, the line-widths and the kinematics of the gas. Also the line detection suppresses the problems of confusion of sources, that can affect the continuum surveys with single dishes.

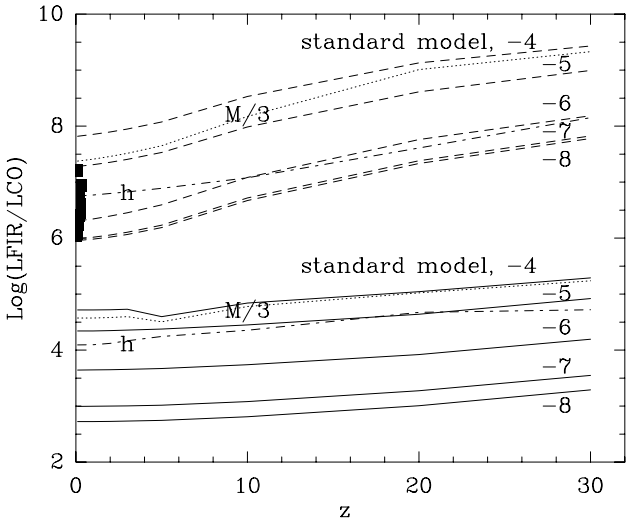

Fig. 9. Luminosity ratio between the total Far infrared (FIR) dust emission and the total integrated CO line emission (full lines), or only the integrated CO(1-0) emission (dashed lines), as a function of redshift. The lines are labeled by the log of CO/H_2 abundance ratio (-4 for the standard model). The dotted lines indicate the result of dividing the gas mass in the standard model by 3 (labeled M/3). The dash-dotted lines correspond to the homogeneous model (labeled h), displayed in Fig. 8. The ratio for the 37 ultra-luminous infrared galaxies observed by Solomon et al. (1997) is marked as filled squares.

We remark that we do not retrieve the surprising result of Silk & Spaans (1997), that the CO lines are even easier to detect than the continuum at very high redshift. From our results, the continuum-to-line flux ratio increases with redshift whatever the model and the optical thickness. In Fig. 2 from Silk & Spaans (1997), the maximum line flux for the CO lines does not vary significantly with redshift from 5 to 30, while we have in all cases a variation as large as $(1+z)^{-2.5}$ in the same range.[2]

5. Detection perspectives

We have computed, for both line and continuum, the integration time required to detect a high-redshift object, with the best possible CO line, or the best continuum frequency. These are displayed in Tables 3 and 4. A signal-to-noise ratio of a factor 5 has been assumed on the continuum flux S_ν, and these estimations have been done for the two-component model of Fig. 4. For the line, the signal-to-noise ratio adopted is 3 when the noise is smoothed over 30 km s^{-1} width, or 9 when smoothed over the whole line width (300 km s^{-1}). Since the sub-mm and mm do-

[2] We can note that they do not take into account the overlapping of clouds on the line of sight, but this is in our model a factor 3 only, and cannot account for the factor ~ 60 discrepancy.

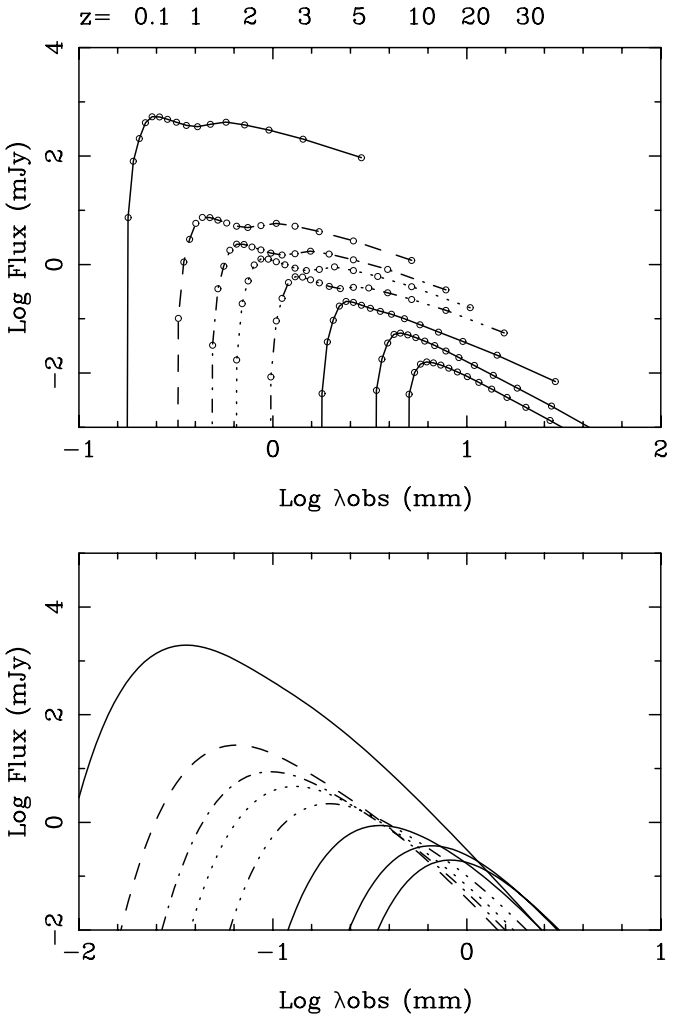

Fig. 10. Same as Fig. 4, but for one optically thin model, with CO/H_2 = 10^{-6}.

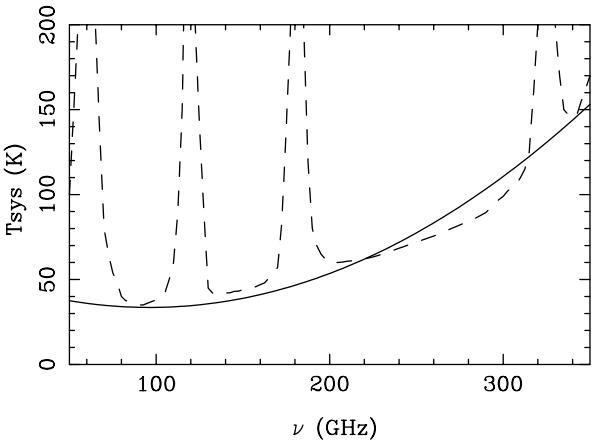

Fig. 11. System temperature as a function of frequency adopted for the LSA/MMA instrument. Dash curve: actual expected T_{sys}, corresponding to a receiver temperature equal to 2 hν/k, operating in full SSB mode, with 1mm height of water, temperature 0° (at altitude 5 km); Full curve: second-order polynomial fit

main is in fact punctuated by transparent atmospheric windows and opaque broad regions, due to O_2 and H_2O, some particular redshifts will be severely disfavored, as for the CO lines detection. We have not taken into account such a complex frequency dependence in our estimations, but on the contrary, we have kept only the upper envelope of atmospheric transmission all over the domain (in Table 3, we have however avoided to estimate integration times exactly at the center of atmospheric lines). The final estimations are therefore valid statistically for a big sample of sources, but can be wrong for a given object for which the best CO lines fall in an opaque atmospheric region. This is not as severe for continuum detections.

For presently operating telescopes, the system temperature is taken from well known measurements between 1 and 3mm, and then extrapolated as a second order polynomial in frequency. For planned instruments, the large foreseen improvement in receivers is taken into account (about a factor 4 in system temperatures, and therefore noise power, cf Guilloteau, 1996). This corresponds to receiver temperatures of the order of 2 $h\nu/k$, and SSB mode (at least 20 dB rejection). For the LSA-MMA project, a configuration of 64 antennae of 12m has been adopted (providing a collecting surface of 7200 m^2). The expected surface efficiency of telescopes and their altitudes are also taken into account. Fig. 11 shows how the 2nd-order polynomial fit corresponds to the lower envelope of the expected T_{sys} for the LSA/MMA. For the continuum, the flux is smoothed over 0.5 and 4 GHz for the IRAM and LSA/MMA interferometers respectively, and 0.1 ν for bolometers. The sensitivity figures given in Table 4 for the continuum receivers have been taken from Holland et al. (1998) for JCMT-Scuba, and from Glenn et al. (1998) for Bolocam. All estimates have been done assuming point sources.

The results in Tables 3 and 4 are of course only orders of magnitude, since they depend on the starburst model, and also the technical performances of planned instruments are only extrapolated. But they give already a good insight in what will be feasible in the next decade. The continuum sources are already detectable with present instruments at all redshifts. Large interferometers will be necessary to reduce the confusion level, and map the sources. The CO lines are presently not detectable easily at redshifts larger than 1. The few detections already published at high z owe their detection to the high magnification factor provided by a gravitational lens, or to exceptionally massive objects. For instance, the actual integrated intensity of BR 1335-0414, 2.8 $\pm$ 0.3 Jy km s^{-1} at $z = 4.4$, Guilloteau et al. 1997) is a factor 9 larger than our standard model at $z = 5$, at 3mm. With the future instruments, they will be detectable easily up to $z = 10$ and may be larger, if huge starbursts exist there. At $z < 5$, it will be possible to detect CO lines from more normal galaxies, and to tackle star formation in those very young galaxies. More exotic lines, such as CS, HCN, or even H_2O will then be available to explore the physics of the interstellar medium and star formation in more detail.

Table 3. Smallest integration time to detect CO lines, (with optimum ν in GHz)

	Present Receivers		Future Receivers		
z	IRAM-30m	IRAM-PdB	GBT-100m	LMT-50m	LSA-MMA
0.1	3mn (209)	1mn (209)	0.4s (105)	1.5s (209)	0.04s (209)
1	36h (230)	16h (230)	4mn (115)	15mn (230)	22s (230)
2	180h (230)	70h (230)	8mn (115)	1h15 (230)	2mn (230)
3	210h (144)	86h (144)	13mn (115)	1h15 (144)	2mn (144)
5	36d (115)	14d (115)	1h (115)	10h (115)	15mn (115)
10	–	–	13h (115)	5d (146)	3h (146)
20	–	–	90h (77)	–	28h (77)
30	–	–	54d (52)	–	15d (52?)

The time is estimated to have a 3σ detection of the flux S_ν, smoothed to 30 km s^{-1}
(one tenth of the profile width of 300 km s^{-1}), equivalent to a 9σ detection, smoothed to 300 km s^{-1}
For all future receivers, T_{sys} has been computed assuming T_{rec} = 2 h ν/k, and 1mm height of water

Table 4. Smallest integration time to detect dust continuum (at 5σ, with optimum λ in μm)

	Present Receivers		Future Receivers		
z	IRAM-30m	JCMT-Scuba	CSO-Bolocam	LMT-Bolocam	LSA-MMA
0.1	6mn (1250)	25s (350)	50s (1100)	0.1s (1100)	36ms (850)
1	6.7h (1250)	1h (450)	55mn (1100)	6s (1100)	2.7s (850)
2	3.9h (1250)	52mn (850)	35mn (1100)	4s (1100)	1.8s (850)
3	2.2h (1250)	38mn (850)	20mn (1100)	2.3s (1100)	1.5s (850)
5	1.1h (1250)	22mn (850)	10mn (1100)	1.2s (1100)	0.9s (1250)
10	24mn (1250)	9mn (850)	4mn (1100)	0.5s (1100)	0.3s (1250)
20	13mn (1250)	19mn (850)	3mn (1100)	0.4s (1100)	0.15s (1250)
30	44mn (1250)	1.2h (1350)	16mn (1100)	1.8s (1100)	0.6s (1250)

The following sensitivities were used, for one second integration time: 50mJy (IRAM-30m at 1250 μm);
1200, 530, 80 and 60mJy (JCMT-Scuba, at 350, 450, 850 and 1350 μm respectively);
30mJy (CSO-Bolocam at 1100 μm); 1.3mJy (LMT-Bolocam at 1100 μm);
2 and 0.7 mJy (LSA-MMA at 850 and 1250 μm, respectively)

Acknowledgements. We thank D. V. Trung for his LVG code, James Lequeux and F. Viallefond for useful discussions, and an anonymous referee for helpful and detailed comments.

References

Barnes J., Hernquist L., 1992, ARA&A 30, 705
Barvainis R., Alloin D., Guilloteau S., Antonucci R., 1998, ApJ 492, L13
Barvainis R., Maloney P., Antonucci R., Alloin D., 1997 ApJ 484, 695
Barvainis R., Tacconi L., Antonucci R., Coleman P., 1994, Nat 371, 586
Benford D.J., Cox P., Omount A., et al., 1999, in prep.
Blain A.W., Longair M.S., 1993, MNRAS 264, 509
Boulanger F., Abergel A., Bernard J-P., et al., 1996, A&A 312, 256
Brown R., Van den Bout P., 1992, ApJ 397, L19
Bryant P.M., Scoville N.Z., 1996, ApJ 457, 678
Downes D., Solomon P.M., Radford S.J.E., 1995, ApJ 453, L65
Downes D., Neri R., Wiklind T., Wilner D.J., Shaver P., 1999, ApJ 513, L1
Draine B.T., Lee H.M., 1984, ApJ 285, 89
Elbaz D., Arnaud M., Casse M., et al., 1992, A&A 265, L29
Frayer D.T., Ivison R.J., Scoville N.Z., et al., 1998, ApJ 506, L7
Frayer D.T., Ivison R.J., Scoville N.Z., et al., 1999, ApJ preprint (astro-ph/9901311)
Glenn J., Bock J.J., Chattopadhyay G., et al., 1998, Proceedings, SPIE International Symposium on Astronomical Telescopes and Instrumentation, Kona, Hawaii, March 1998 (http://astro.caltech.edu/ lgg/bolocam/bins.html)
Gordon M.A., Baars J.W.M., Cocke W.J., 1992, A&A 264, 337
Guiderdoni B., Hivon E., Bouchet F.R., Maffei B., 1998, MNRAS 295, 877
Guilloteau S., Omont A., McMahon R.G., Cox P., PetitJean P., 1997, A&A 328, L1
Guilloteau S., 1996, LSA memo 001 (http://iram.fr/LSA/collab-mma/reports/reports.html)
Hughes D.H., Serjeant S., Dunlop J., et al., 1998, Nat 394, 241
Holland W.S., Robson E.I., Gear W.K, et al., 1998, MNRAS in press (astro-ph/9809122)
Israel F.P., van der Werf P.P., 1996, In: Bremer M.N., van der Werf P.P., Röttgering H.J.A., Carilli C.L. (eds.) Cold gas at high redshift. Kluwer, p. 429
Klaas U., Haas M., Heinrichsen I., Schulz B., 1997, A&A 325, L21
Madau P., Ferguson H.C., Dickinson M.E., et al., 1996, MNRAS 283, 1388
McMahon R.G., Omont A., Bergeron J., Kreysa E., Haslam C.G.T., 1994, MNRAS 267, L9
Norman C.A., Braun R., 1996, In: Bremer M.N., van der Werf P.P., Röttgering H.J.A., Carilli C.L. (eds.) Cold gas at high redshift. Kluwer, p. 3

Ohta K., Yamada T., Nakanishi K., et al., 1996, Nat 382, 426
Oke J.B., Sandage A., 1968, ApJ 154, 21
Omont A., Petitjean P., Guilloteau S., McMahon R.G., Solomon P.M., 1996a, Nat 382, 428
Omont A., McMahon R.G., Cox P., et al., 1996b, A&A 315, 10
Scoville N.Z., Yun M.S., Bryant P.M., 1997a, ApJ 484, 702
Scoville N.Z., Yun M.S., Windhorst R.A., Keel W.C., Armus L., 1997b, ApJ 485, L21
Scoville N.Z., Sargent A.I., Sanders D.B., Soifer B.T., 1991, ApJ 366, L5
Silk J., Spaans M., 1997, ApJ 488, L79
Solomon P.M., Downes D., Radford S.J.E., 1992a, Nat 356, 318
Solomon P.M., Downes D., Radford S.J.E., 1992b, ApJ 387, L55
Solomon P.M., Downes D., Radford S.J.E., Barrett J.W., 1997, ApJ 478, 144
Solomon P.M., Radford S.J.E., Downes D., 1990, ApJ 348, L53
Weinberg S., 1972, Gravitation and Cosmology. John Wiley & Sons, New York